Nanoscale

PAPER

View Article Online
View Journal | View Issue

Cite this: *Nanoscale*, 2015, **7**, 17836

Cell-specific optoporation with near-infrared ultrafast laser and functionalized gold nanoparticles†

Eric Bergeron,[a] Christos Boutopoulos,[a,b] Rosalie Martel,[a] Alexandre Torres,[a] Camille Rodriguez,[a] Jukka Niskanen,[c] Jean-Jacques Lebrun,[d] Françoise M. Winnik,[c,e] Przemyslaw Sapieha[f] and Michel Meunier*[a]

Selective targeting of diseased cells can increase therapeutic efficacy and limit off-target adverse effects. We developed a new tool to selectively perforate living cells with functionalized gold nanoparticles (AuNPs) and near-infrared (NIR) femtosecond (fs) laser. The receptor CD44 strongly expressed by cancer stem cells was used as a model for selective targeting. Citrate-capped AuNPs (100 nm in diameter) functionalized with 0.01 orthopyridyl-disulfide-poly(ethylene glycol) (5 kDa)-*N*-hydroxysuccinimide (OPSS-PEG-NHS) conjugated to monoclonal antibodies per nm^2 and 5 μM HS-PEG (5 kDa) were colloidally stable in cell culture medium containing serum proteins. These AuNPs attached mostly as single particles 115 times more to targeted CD44$^+$ MDA-MB-231 and CD44$^+$ ARPE-19 cells than to non-targeted CD44$^-$ 661W cells. Optimally functionalized AuNPs enhanced the fs laser (800 nm, 80–100 mJ cm^{-2} at 250 Hz or 60–80 mJ cm^{-2} at 500 Hz) to selectively perforate targeted cells without affecting surrounding non-targeted cells in co-culture. This novel highly versatile treatment paradigm can be adapted to target and perforate other cell populations by adapting to desired biomarkers. Since living biological tissues absorb energy very weakly in the NIR range, the developed non-invasive tool may provide a safe, cost-effective clinically relevant approach to ablate pathologically deregulated cells and limit complications associated with surgical interventions.

Received 19th August 2015,
Accepted 19th September 2015

DOI: 10.1039/c5nr05650k

www.rsc.org/nanoscale

1. Introduction

Gold nanoparticles (AuNPs) have found numerous applications in nanomedicine and medical diagnostics, in view of their robustness, ease of functionalization and low toxicity.[1,2] They are particularly well-suited for optical treatment of cancer tumors, due to their photostability and their ability to display localized surface plasmon resonance, a collective oscillation of electrons from the conduction band when excited by a laser irradiation at a specific wavelength. For example, AuNPs (100 nm in diameter) exhibit strong absorption resonance for incident wavelengths around 570 nm in water.[3] Laser treatment using on-resonant irradiation of AuNPs in different shapes has been widely employed for cell nanosurgery applications based on localized phenomena induced by AuNP heating.[4,5] Off-resonance laser irradiation of spherical AuNPs (*e.g.*, λ = 800 nm for 100 nm AuNPs) minimizes the heat absorption from AuNPs and biological tissues since they absorb energy very weakly between 650 and 900 nm, in the near-infrared (NIR) range.[6,7] Upon AuNP irradiation by an off-resonance NIR femtosecond (fs) laser, the local amplification of the electromagnetic field around the AuNP can cause the generation of nanoplasma and eventually a nanobubble around the AuNP, thus inducing cell perforation without AuNP fragmentation.[7–10] Our group has demonstrated that off-resonance NIR fs laser excitation at 800 nm of 100 nm citrate-capped AuNPs enables high cell membrane perforation, while maintaining high cell viability

[a]*Laser Processing and Plasmonics Laboratory, Department of Engineering Physics, Polytechnique Montréal, C.P. 6079, Succursale Centre-ville, Montreal, QC H3C 3A7, Canada. E-mail: michel.meunier@polymtl.ca*
[b]*SUPA, School of Physics and Astronomy, University of St. Andrews, North Haugh, St. Andrews, KY16 9SS, UK*
[c]*Faculty of Pharmacy and Department of Chemistry, Université de Montréal, C.P. 6128, Succursale Centre-ville, Montreal, QC H3C 3J7, Canada*
[d]*Division of Medical Oncology, Department of Medicine, McGill University Health Centre, Montreal, QC H3A 1A1, Canada*
[e]*World Premier International (WPI) Research Center Initiative, International Center for Materials Nanoarchitectonics (MANA) and National Institute for Materials Science (NIMS), 1-1 Namiki, Tsukuba, Ibaraki, 305-0044, Japan*
[f]*Department of Ophthalmology, Hôpital Maisonneuve-Rosemont Research Center, Université de Montréal, Montreal, QC H1T 2M4, Canada*

† Electronic supplementary information (ESI) available: Characterization of functionalized gold nanoparticles by UV-visible-NIR spectroscopy and zeta potential measurements; selectivity of cell targeting with functionalized gold nanoparticles by immunofluorescence, flow cytometry and scanning electron microscopy; selective treatment of targeted cells with functionalized gold nanoparticles and ultrafast laser. See DOI: 10.1039/c5nr05650k

and enabling transfection of DNA plasmids into human cancer cells.[8] The next step for selective cell optoporation is to develop stable AuNPs which target cancer cells in cell culture medium containing serum proteins without affecting surrounding non-targeted cells. Here we report a novel *in vitro* approach for efficient targeting and NIR fs laser-induced perforation of cancer cells using 100 nm AuNPs decorated with monoclonal antibodies (Abs) that target CD44 receptors that are widely overexpressed in many types of cancers.

It is well established that molecular targeting of AuNPs coated with poly(ethylene glycol) (PEG) towards cell surface markers enhances their accretion on targeted cells, increases their circulation half-life, and consequently decreases the required dosage of AuNPs.[11] Abs are commonly conjugated to the surface of AuNPs by heterobifunctional PEG linkers (PEG-Ab) given their high affinity for many established biomarkers.[2,12,13] AuNPs functionalized with different Abs have been used to target cancer cells expressing different receptors, such as the epidermal growth factor receptor (EGFR),[14] the epidermal growth factor receptor-2 (HER2),[15–17] the epithelial cell adhesion molecule (EpCAM),[18] the fibroblast activation protein-α (FAP-α),[19] and the cluster of differentiation 44 (CD44).[20,21] Cancer cells overexpressing the cell surface glycoprotein CD44 are usually associated with a cancer stem cell-like (CSC) phenotype. Even though CSCs represent only a fraction of the total cancer cell population within the tumor, these cells are largely responsible for tumor aggressivity, invasiveness and metastasis, due to their self-renewal potential and ability to generate all the differentiated cancer cell types within the tumor. Moreover, partly due to a slower proliferative rate and higher expression levels of ABC transporters and drug efflux, CSCs are usually highly resistant to radiotherapy and chemotherapy, which mainly target differentiated and highly proliferative tumor cells.[22] A $CD44^+$ phenotype correlates with the presence of CSCs in breast, bone, colorectal, prostate, pancreas, head and neck cancers.[23] $CD44^+$ tumors are associated with the induction of metastasis and decreased survival for patients with breast cancer.[24] The CD44 cell surface marker is thus an ideal target to selectively identify breast CSCs.[25] Similarly to tumorigenic human breast cancer cells,[26] MDA-MB-231 cells express surface markers of breast CSCs (87% of these cells are $CD44^+$, mainly expressing the CD44s standard isoform),[27] and have all their characteristics.[28] $CD44^+$ MCF7 human breast cancer cell-engineered mammospheres have been previously targeted with gold nanorods functionalized with HS-PEG(3.4 kDa)-Ab in the absence of HS-PEG and treated with a NIR diode laser.[21]

For optosurgery applications, AuNPs must be sufficiently large (100–150 nm in diameter) to ensure the efficient near-field enhancement and nanoplasma formation necessary to perforate living cells.[4,7] Large AuNPs are difficult to stabilize by steric repulsion of ligands, such as PEG chains, given their large Hamaker constant and resulting van der Waals interactions that outweigh the steric repulsion afforded by PEG chains.[18] Low-molecular weight PEG offers high bioconjugation yields, while high-molecular weight PEG provides excellent steric protection. Very high binding affinity to breast cancer cells of AuNPs ranging in diameter from 15 to 175 nm was achieved by tethering HS-PEG layers with low- and high-molecular weight PEG chains conjugated to anti-EpCAM Abs in carefully selected molar ratios.[18] In addition, the protocol employed to mix PEG-Ab and PEG chains of different lengths and concentrations also affects the ultimate targeting efficiency of Ab-functionalized AuNPs. For example, Lowery and colleagues functionalized AuNPs sequentially with Abs end-linked to orthopyridyl-disulfide-PEG(2 kDa)-*N*-hydroxysuccinimide (OPSS-PEG(2 kDa)-NHS), followed by HS-PEG (5 kDa) to effectively target $HER2^+$ SK-BR-3 breast cancer cells.[16] Chattopadhyay and colleagues also targeted SK-BR-3 cells with anti-HER2 Abs, but the protocol reported in this study calls for simultaneous addition to AuNPs of OPSS-PEG(5 kDa)-Ab and shorter HS-PEG (2 kDa).[15] These functionalized AuNPs in combination with X-rays enhanced DNA double strand cleavage in targeted cells, compared to X-radiation alone, thus improving the radiotherapy treatment.[15] We previously used functionalized AuNPs with OPSS-PEG(5 kDa)-Ab and HS-PEG (2 or 5 kDa) for imaging of $CD44^+$ MDA-MB-231 cancer cells, but we did not evaluate their stability under physiological conditions of pH and salinity.[29] The stability of functionalized AuNPs is critical for selective optoporation since serum proteins in the cellular environment can adsorb non-specifically on AuNPs.[30]

Here AuNPs were functionalized with mixed PEG layers combining different ratios of HS-PEG (2 or 5 kDa) and OPSS-PEG(5 kDa)-Ab targeting the CD44 cell surface receptor. The NHS end function of OPSS-PEG-NHS was coupled to monoclonal anti-CD44 Ab's amine residues through an amide linkage to provide great conformational freedom and improve its efficiency for binding with the targeted CD44 biomarker (Fig. 1). The OPSS end's disulfide group of this OPSS-PEG-Ab complex is known to bind strongly to the AuNP surface.[13] The remaining free sites on the AuNPs were blocked with thiolated PEG chains which can assemble into a densely packed coating. The stability of functionalized AuNPs was evaluated in cell culture medium containing serum proteins. The selective targeting with stable functionalized AuNPs was assessed on $CD44^+$ human cells (MDA-MB-231 (CSC-like phenotype) and ARPE-19) and on non-targeted $CD44^-$ 661W cells. Selective optoporation of these cells was evaluated as a function of NIR fs laser parameters (fluence, repetition rate) and functionalized AuNPs concentration. Then, optimally functionalized AuNPs and laser parameters were used to demonstrate selective optoporation of targeted cells without affecting surrounding non-targeted cells in co-culture.

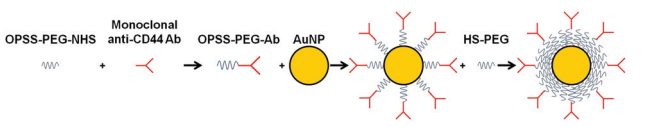

Fig. 1 Schematic representation of AuNPs functionalized with mixed PEG layers and monoclonal anti-CD44 Abs.

2. Results and discussion

2.1. Preparation of stable functionalized AuNPs suitable for optoporation

The first part of this study was devoted to the optimization of the composition of the AuNPs outer shell and the development of an appropriate synthesis protocol. Commercial citrate-capped AuNPs at 50 μg mL^{-1} aggregate rapidly upon treatment with 1% (w/v) aqueous NaCl, a solution that is approximately isotonic with normal human plasma (290 mOsm kg^{-1}).[31] Aggregation is detected readily by monitoring the intensity of the plasmon band of the AuNPs. After 30 min, the plasmon band intensity of AuNPs in saline environment decreased by 69 ± 3%, compared to AuNPs dispersed in water (Fig. S1A,B†). PEGylation of AuNPs with HS-PEG (2 or 5 kDa) triggered a 2.4 ± 0.8 nm and 2.8 ± 0.6 nm red-shift of the plasmon band, respectively (from ~570 nm to ~572.5 nm) with no loss of intensity (Fig. S1A,B†). Based on Mie theory,[3] the maximum of the plasmon band for 100 nm AuNPs in water should be 569 nm, a value close to the experimental result. The ~2.5 nm shift to longer wavelength observed upon PEGylation corresponds to an outer shell thickness of ~2 nm around AuNPs, attributed to the presence of adsorbed thiolated PEG chains (n = 1.459).[3,18,32] Treatment of AuNPs with HS-PEG (2 or 5 kDa) at a concentration of 1 μg mL^{-1} or higher enhanced significantly the stability of AuNPs in 1% NaCl, but the resistance of AuNPs against aggregation in saline environment was lost when the HS-PEG concentration was 0.1 μg mL^{-1} or less (p < 0.001, Fig. 2A and S1A,B†).

After one day incubation in 1% NaCl, the normalized plasmon peak intensity of citrate-capped AuNPs decreased to 23 ± 5%. A similar intensity loss occurred also in the case of AuNPs treated with less than 0.1 μg mL^{-1} HS-PEG (Fig. 2A and S1C,D†). AuNPs treated with HS-PEG of higher concentration were more stable, especially in the case of HS-PEG (5 kDa) (10 μg mL^{-1} or higher, p < 0.001, Fig. 2A and S1C,D†). Assuming a 0.35 nm^2 footprint of HS-PEG (5 kDa) on the Au surface,[33] one can calculate that 5.71 × 10^9 AuNPs per mL each containing 89 760 sites per AuNP can be saturated with 3.8 μg mL^{-1} HS-PEG (5 kDa). In the experiments described below, HS-PEG was added at a concentration of 5 μM, which corresponds to 7.3 thiolated PEG chains for each site available on the Au surface, taking into account the 10% dilution from OPSS-PEG-Ab.

AuNPs were functionalized with anti-CD44 Abs to ensure targeting of cells overexpressing the CD44 receptor. The Abs were linked to OPSS-PEG(5 kDa)-NHS (OPSS-PEG-Ab) incorporated at a level of 0.45% (v/v) to the AuNPs. The mixed corona was prepared by sequential treatment of citrate-capped AuNPs with OPSS-PEG-Ab, followed by HS-PEG (2 or 5 kDa) or incubation of citrate-capped AuNPs with a mixture of OPSS-PEG-Ab and HS-PEG (2 or 5 kDa). The stability of AuNPs functionalized with different PEG chain lengths and mixing conditions was analyzed by monitoring changes in the Au plasmon band. After 30 min incubation in water, the normalized plasmon peak intensity of functionalized AuNPs decreased slightly, ranging between 88 and 100%, depending on the preparation

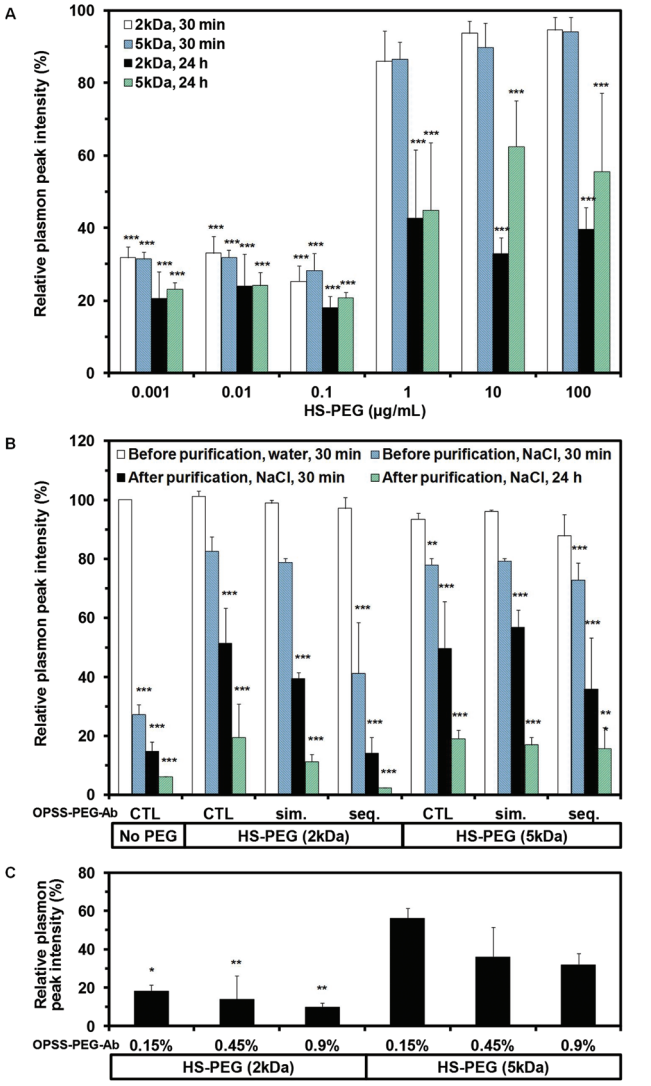

Fig. 2 Normalized plasmon peak absorbance measured by UV-visible-NIR spectroscopy of functionalized AuNPs. (A) AuNPs functionalized with increasing amounts of HS-PEG (2 or 5 kDa, 0.001 to 100 μg mL^{-1}) were incubated in 1% NaCl for 30 min or 24 h. Results are expressed as means ± standard deviation (SD) from five independent experiments. Statistically significant differences are indicated by ***p < 0.001 in comparison to citrate-capped AuNPs incubated in water. (B) AuNPs were functionalized with (i) HS-PEG (2 or 5 kDa), (ii) OPSS-PEG-Ab (0.45%) simultaneously (sim.) with HS-PEG or (iii) OPSS-PEG-Ab (0.45%) during 1 h sequentially (seq.) followed by HS-PEG. Samples were incubated before or after purification with water or 1% NaCl for 30 min or 24 h. Control: CTL. Results are expressed as means ± SD from six independent experiments. Statistically significant differences are indicated by **p < 0.01 and ***p < 0.001 in comparison to citrate-capped AuNPs incubated in water. (C) AuNPs were functionalized with OPSS-PEG-Ab (0.15, 0.45 or 0.9%) during 1 h sequentially followed by HS-PEG (2 or 5 kDa). Samples were incubated after purification with 1% NaCl for 30 min. Results are expressed as means ± SD from three independent experiments. Statistically significant differences are indicated by *p < 0.05 and **p < 0.01 in comparison to AuNPs functionalized with OPSS-PEG-Ab (0.15%) and HS-PEG (5 kDa).

protocol (Fig. 2B and S2A†). Addition of 1% NaCl caused aggregation of the AuNPs functionalized sequentially with OPSS-PEG-Ab and HS-PEG (2 kDa) (Fig. S2B†), and the normalized intensity of the plasmon band decreased to 41% (Fig. 2B). The sequential functionalization of AuNPs with OPSS-PEG-Ab and the longest PEG chain (5 kDa) resulted in a normalized intensity ratio of 73%. This ratio was 79% for AuNPs functionalized with a mixture of OPSS-PEG-Ab and HS-PEG (2 or 5 kDa), similarly to PEGylated AuNPs.

Batches of functionalized AuNPs were subjected to centrifugation immediately after synthesis in order to isolate the AuNPs and suspend them in phenol red-free Dulbecco's Modified Eagle's Medium (DMEM), the cell culture medium used in the *in vitro* tests described below. After 30 min incubation in either water or 1% NaCl, the normalized plasmon peak intensity of purified AuNPs functionalized sequentially with OPSS-PEG-Ab and HS-PEG (2 kDa) decreased to 15% (Fig. 2B and S2C,D†). The normalized intensity ratio decreased to 50% for PEGylated AuNPs with either 2 or 5 kDa, to 36% for AuNPs covered with sequential addition of OPSS-PEG-Ab and HS-PEG (5 kDa), and to 39% and 57% for AuNPs covered simultaneously with OPSS-PEG-Ab and HS-PEG (2 or 5 kDa), respectively. One day after purification, the normalized plasmon peak intensity decreased to 20% for PEGylated AuNPs, and to 11–17% for AuNPs functionalized simultaneously with OPSS-PEG-Ab and HS-PEG. AuNPs functionalized sequentially with OPSS-PEG-Ab and HS-PEG (2 or 5 kDa) had a normalized plasmon peak intensity decreasing to 2% and 16%, respectively (Fig. 2B). These results indicate that CD44-targeted AuNPs covered sequentially with OPSS-PEG-Ab and HS-PEG (5 kDa) are more stable in a saline environment than those obtained with HS-PEG (2 kDa), either before purification or after centrifugation and suspension in cell culture medium. Unpurified AuNPs functionalized sequentially with OPSS-PEG-Ab and HS-PEG (5 kDa) remained stable up to three months at 4 °C (data not shown).

The zeta potential of AuNPs (citrate-capped, PEGylated or functionalized by sequential addition of OPSS-PEG-Ab (0.45%) and HS-PEG (2 or 5 kDa)) was determined at 4, 20 and 37 °C. The citrate-capped AuNPs had a negative zeta potential (∼−41 mV). The zeta potentials of PEGylated AuNPs with HS-PEG (2 or 5 kDa) increased to ∼−20 and −11 mV, respectively, independently of the temperature and of the presence, or not, of Abs. Exact values of zeta potentials for all AuNPs and temperatures are given in Fig. S3.† These values are consistent with the expected transition from electrostatic stabilization of citrate-capped AuNPs to mostly steric stabilization in the case of PEGylated AuNPs,[34] thus confirming the successful functionalization of the AuNPs.

Previous reports have indicated that the use of functionalized AuNPs affects the targeting efficiency. The optimal OPSS-PEG-Ab : HS-PEG ratio for high targeting efficiency varies with the size and the shape of the AuNPs and the reaction conditions.[2] For example, Morton and colleagues suggest that, for optimal targeting efficiency, the OPSS-PEG-Ab density on the AuNP corona should be ∼0.02 OPSS-PEG-Ab per nm^2.[35] By using solutions of OPSS-PEG-Ab (0.9, 0.45 and 0.15% (v/v)) and HS-PEG (2 or 5 kDa) in performing the sequential functionalization protocol, we prepared AuNPs with OPSS-PEG-Ab density of 0.02, 0.01, and 0.00333 OPSS-PEG-Ab per nm^2, so that there should be on average from 658 to 110 OPSS-PEG-Ab chains in the corona surrounding each 100 nm AuNP (Table S1†). The outcome of the functionalization was monitored by measuring the intensity and the position of the AuNP plasmon band for aliquots in water of suspensions obtained immediately at the end of the synthesis. The plasmon band exhibited a red-shift of about 0.5 ± 0.2, 1.8 ± 0.3 and 2.5 ± 0.2 nm for OPSS-PEG-Ab (0.15, 0.45 and 0.9%), respectively, compared to the plasmon band of the citrate-capped AuNPs (Fig. S4A†). In a saline environment, the intensity of the band recorded for AuNPs functionalized with different concentrations of OPSS-PEG-Ab and HS-PEG (2 kDa) strongly decreased (Fig. S4B†). Only a slight decrease in plasmon band intensity was observed for AuNPs functionalized with OPSS-PEG-Ab and HS-PEG (5 kDa) (Fig. S4B†). The highest plasmon band intensity of purified functionalized AuNPs in either water or 1% NaCl was recorded in the case of AuNPs functionalized with OPSS-PEG-Ab (0.15%) in combination with HS-PEG (5 kDa) (Fig. 2C and S4C,D†). Interestingly, the plasmon band intensity decreased slightly by increasing OPSS-PEG-Ab concentration in the presence of HS-PEG (2 kDa) (Fig. 2C and S4C,D†).

2.2. *In vitro* targeting assay

The second part of this study aimed to demonstrate successful cell targeting with stable functionalized AuNPs in the presence of serum proteins. Suspensions in DMEM of functionalized AuNPs isolated by centrifugation immediately after preparation were added to CD44$^+$ MDA-MB-231 cells cultured in DMEM containing 10% (v/v) fetal bovine serum (FBS).[28] After 3 h incubation, the cells were washed three times with phosphate-buffered saline (PBS) to remove unbound AuNPs.[8,10,36] The cells were fixed and stained with 4′,6-diamidino-2-phenylindole dihydrochloride (DAPI), a blue-emitting dye used to visualize the cell nucleus by fluorescence imaging. The cells were also observed by darkfield microscopy, which detects light elastically scattered by AuNPs. The two micrographs were combined in the images presented in Fig. 3.

In darkfield imaging, cell membranes were detected by the white light they scattered (Fig. 3A). AuNPs scattered light more efficiently. They were readily detected by the slightly orange scattered light in darkfield microscopy as seen in Fig. 3B, which presents the combined micrographs recorded for MDA-MB-231 cells treated with citrate-capped AuNPs. These AuNPs randomly bound to the cell membrane and to the glass substrate. Micrographs of MDA-MB-231 cells treated with PEGylated AuNPs are presented in Fig. 3D (HS-PEG 2 kDa) and Fig. 3H (HS-PEG 5 kDa). Only a few AuNPs can be seen on the images, indicating that non-specific interactions between the AuNPs and the cells were mostly shielded by the PEG corona of the AuNPs. Micrographs of MDA-MB-231 cells treated with PEGylated AuNPs obtained by sequential addition of OPSS-PEG-Ab and HS-PEG (2 or 5 kDa) (Fig. 3F and J) pre-

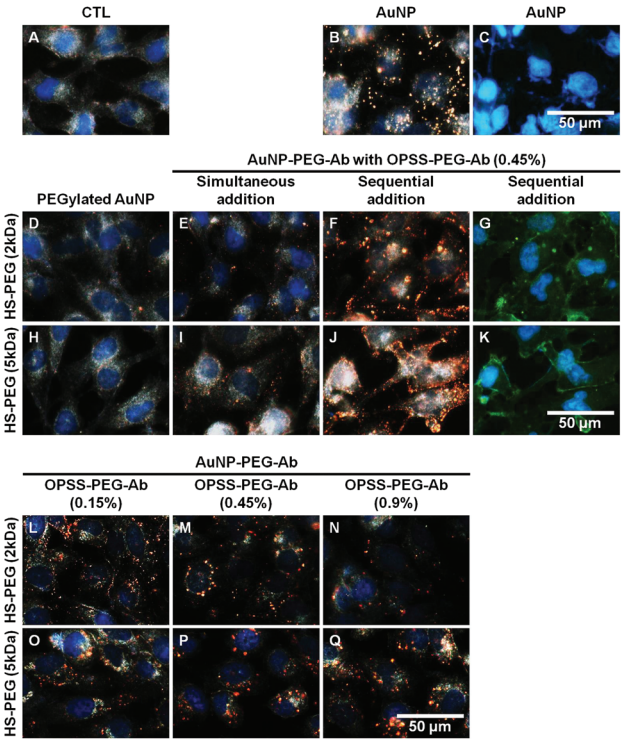

Fig. 3 Darkfield and fluorescence imaging of CD44$^+$ MDA-MB-231 cells incubated for 3 h in DMEM/10% FBS/1% PS without (A) or with 8 µg mL^{-1} citrate-capped AuNPs (B–C) or functionalized AuNPs (D–Q). AuNPs were functionalized with (i) HS-PEG (2 or 5 kDa) (D,H), (ii) OPSS-PEG-Ab simultaneously with HS-PEG (E,I) or (iii) OPSS-PEG-Ab (0.15, 0.45 or 0.9%) during 1 h sequentially followed by HS-PEG (F,G,J–Q). The darkfield and fluorescence images were combined, except for fluorescence images showing the detection of anti-CD44 Abs with green-emitting Alexa Fluor 488 dye conjugated to goat anti-rat IgG Abs (C,G,K). Cell nuclei were stained with DAPI (blue). Representative images were obtained from two independent experiments.

sented large domains of bright orange scattered light due to AuNPs bound to the surface of the cells, presumably by virtue of specific interactions between the Ab-modified AuNPs and the CD44 receptors on the cell surfaces. The signal observed was stronger in the case of cells treated with OPSS-PEG-Ab and HS-PEG (5 kDa), compared to cells treated with OPSS-PEG-Ab and HS-PEG (2 kDa). MDA-MB-231 cells treated with functionalized AuNPs prepared by simultaneous addition of OPSS-PEG-Ab and HS-PEG (2 or 5 kDa) to AuNPs were also imaged by darkfield microscopy. As seen in Fig. 3E and I, only a few AuNPs adhered to the cell surfaces, thus indicating that the Ab fragments were either buried within the PEG corona during the synthesis, or that only a small fraction of the OPSS-PEG-Ab ligands adsorbed on the AuNP surface under conditions of competitive adsorption of excess HS-PEG. *In vitro* assays were conducted with AuNPs of varying OPSS-PEG-Ab density (Fig. 3L–Q). AuNPs functionalized sequentially with OPSS-PEG-Ab (0.45 or 0.9%) and HS-PEG (5 kDa) produced the strongest light scattering amongst all the tested experimental conditions (Fig. 3P and Q).

The Ab activity of functionalized AuNPs bound to CD44$^+$ MDA-MB-231 cells was evaluated by post-treatment of the cells incubated with AuNPs bearing anti-CD44 Abs (such as those presented in Fig. 3F and J) with Alexa Fluor 488 dye conjugated to goat anti-rat IgG Abs. The characteristic green emission of the dye was detected in micrographs of CD44-targeted AuNPs attached to MDA-MB-231 cells (Fig. 3G and K), located mostly on the cell periphery. The green emission colocalized with the bright dot patterns of light scattered by AuNPs visualized by darkfield microscopy (Fig. 3F, G, J and K). Thus, the Abs linked to the AuNPs remained active for cell targeting in the cell culture medium containing serum proteins. Green emission was not observed on micrographs of cells treated under the same conditions with citrate-capped AuNPs, rather than functionalized AuNPs (Fig. 3C).

2.3. Selectivity of cell targeting in medium containing 10% FBS

The third part of this study aimed to demonstrate selective cell targeting with stable functionalized AuNPs. The selectivity of Ab-functionalized AuNPs towards CD44 was evaluated by using two human cell lines that express CD44 (CD44$^+$ MDA-MB-231 breast cancer and CD44$^+$ ARPE-19 retinal pigmented epithelium) and a control cell line (mouse CD44$^-$ 661W photoreceptor) devoid of CD44 receptors. Immunostaining with monoclonal anti-CD44 Abs confirmed the strong expression of CD44 on MDA-MB-231 and ARPE-19 cells (Fig. 4A and B),[28] while 661W cells did not express this receptor after fixation with 70% methanol/30% acetone (Fig. 4C). Similarly, OPSS-PEG-Ab was detected only on targeted cells (Fig. S5A–C†). Cells fixed with 4% paraformaldehyde diluted in PBS led to similar observations (data not shown). Background signal from secondary Abs was not observed in the absence of primary Abs (Fig. S5D–F†). The cells were treated with Ab-functionalized AuNPs as well as citrate-capped AuNPs used as negative controls (Fig. 4D–O, S6, S7 and S8†). Functionalized AuNPs were detected on cells expressing CD44 by darkfield microscopy as well as by fluorescence microscopy, using fluorescent labelling of the anti-CD44 Abs (Fig. 4D–I). In contrast, citrate-capped AuNPs were observed on all cell lines, randomly distributed over the entire area visualized, indicative of non-specific attachment (Fig. S6A–F†).

The selective targeting of functionalized AuNPs to CD44$^+$ cells was confirmed by flow cytometry analysis of the three cell lines treated with Ab-functionalized AuNPs produced by sequential attachment of OPSS-PEG-Ab (0.45%) and HS-PEG (5 kDa) (Fig. S7†). Cells tagged with these AuNPs were detected by the intensity of the light scattered by bound AuNPs. The mean forward scattering intensity of CD44$^+$ MDA-MB-231 and CD44$^+$ ARPE-19 cells increased by 3583 and 4220 with functionalized AuNPs in comparison to cells without AuNPs, respectively, while it remained unchanged for CD44$^-$ 661W cells (Table S2†). The normalized scattered light intensity of targeted MDA-MB-231 and ARPE-19 cells increased 2.6 times after treatment with functionalized AuNPs ($p < 0.001$), while it remained unmodified in non-targeted 661W cells (Fig. 4J–L,

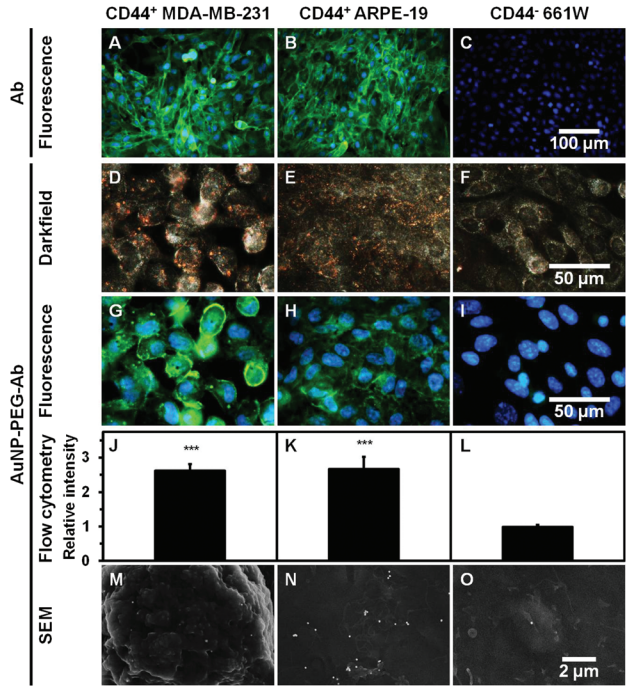

Fig. 4 Selective targeting of cells incubated for 3 h in DMEM/10% FBS/1% PS with 8 µg mL^{-1} AuNPs functionalized with OPSS-PEG-Ab (0.45%) during 1 h sequentially followed by HS-PEG (5 kDa). (A–C) Immunofluorescence of CD44 cell surface receptors in CD44^{+} MDA-MB-231, CD44^{+} ARPE-19 and CD44^{-} 661W cells. Representative images were obtained from five independent experiments. Darkfield (D–F) and fluorescence (G–I) imaging of cells with functionalized AuNPs. Representative images were obtained from two independent experiments. Anti-CD44 Abs were detected with green-emitting Alexa Fluor 488 dye conjugated to goat anti-rat IgG Abs and cell nuclei were stained with DAPI (blue, A-C,G-I). (J–L) Mean forward scattering intensity of cells with functionalized AuNPs was recorded by flow cytometry and normalized to cells without AuNPs for each cell type. Results are expressed as means ± SD from four independent experiments. Statistically significant differences are indicated by ***$p < 0.001$ in comparison to CTL. (M–O) Scanning electron microscopy (SEM) of cells with functionalized AuNPs.

Table S3†). The normalized scattered light intensity of the three cell lines treated with citrate-capped AuNPs increased by a factor of 1.8–2.1 (Table S3†). Cell viability evaluated by the trypan blue exclusion assay remained higher than 89% for cells incubated with functionalized AuNPs during 3 h (Table S4†). Taken together, these data provide strong evidence for selective targeting of CD44^{+} cells with the functionalized AuNPs.

Next, we evaluated the distribution and aggregation status of AuNPs on the cells by SEM of cells incubated with AuNPs, washed with PBS, and fixed (Fig. 4M–O and S8†). Ab-functionalized AuNPs were mostly distributed as single particles on the targeted cells (81% for MDA-MB-231, 66% for ARPE-19). A few small AuNP clusters (<8 AuNPs) were observed as well (Fig. 4M and N). Interestingly, 33% and 58% of the initial functionalized AuNPs were observed on MDA-MB-231 and ARPE-19 cells, respectively, while only 0.3% of these AuNPs were observed on 661W cells. Functionalized AuNPs attached 115 times more to targeted MDA-MB-231 and ARPE-19 cells than to non-targeted 661W cells. Thus, 229 ± 263, 237 ± 67 and 2 ± 3 functionalized AuNPs were observed on MDA-MB-231, ARPE-19 and 661W cells, respectively (Table S5†). Micrographs of cells treated with unpurified and purified citrate-capped AuNPs are presented in Fig. S8.† For the three cell lines, half of the unpurified AuNPs remained as single units, while a similar fraction of AuNPs formed small clusters (<50 AuNPs) (Fig. S8A–C†). In the case of purified AuNPs, large micrometric clusters, containing up to 210 AuNPs, were observed on the cell surface (Fig. S8D–F†). SEM observations indicate the high efficiency of functionalized AuNPs in selective cell targeting. They also demonstrate that functionalized AuNPs do not form large aggregates even in the cell culture medium containing serum proteins. The heterogeneous spatial distribution of CD44 receptors on the cell membrane can explain the presence of small clusters of CD44-targeted AuNPs.[37]

2.4. Selective laser treatment of targeted cells in medium containing 10% FBS

The fourth part of this study was devoted to the optimization of the perforation of targeted cells without affecting non-targeted cells with NIR fs laser and functionalized AuNPs, and the demonstration of selective optoporation with co-cultured targeted and non-targeted cells. The perforation of viable cells with ultrafast laser enhanced by AuNPs requires the optimization of various parameters, such as the laser fluence, the laser repetition rate, the number of laser pulses, the sample speed displacement, the concentration of AuNPs and the incubation time of AuNPs with cells. Our previous work demonstrated that 8 µg mL^{-1} citrate-capped AuNPs and 45 fs NIR laser (800 nm, 1 kHz, 60 mJ cm^{-2}) can perforate human WM278 melanoma cells in a dish moving with a scanning velocity of 3.5 mm s^{-1}.[8] We recently reported the perforation of MDA-MB-231 cells with citrate-capped AuNPs and single 45 fs NIR laser pulse at 800 nm and a repetition rate of 3 Hz.[38] It was found that the bubble generation and cell perforation threshold was 50 mJ cm^{-2} for clustered AuNPs and 75 mJ cm^{-2} for single AuNPs.[38] Based on these results, we explored a laser fluence range of 60–100 mJ cm^{-2}, a repetition rate range of 100–1000 Hz and Ab-functionalized AuNP concentration from 1 to 8 µg mL^{-1} for selective cell treatment with 45 fs NIR laser at 800 nm. In the absence of AuNPs, the viability of irradiated cells stained with DAPI (blue channel) was unaffected with 80–100 mJ cm^{-2} at 250 Hz (Fig. S9A–D†) or 60–80 mJ cm^{-2} at 500 Hz (Fig. S9E–H†). The horizontal scanning of the laser at 100 mJ cm^{-2} (500 Hz) induced the detachment of the three cell lines in the highest energetic laser area, *i.e.* the centre of the Gaussian beam, with the strongest effect for 661W cells (Fig. S9I–K†). The membrane impermeable green fluorescent dye Lucifer Yellow (LY) was taken up weakly with 100 mJ cm^{-2} (250 Hz) or 80 mJ cm^{-2} (500 Hz), and much more strongly with 100 mJ cm^{-2} (500 Hz) in the laser-treated area (Fig. S9C, D,G–K†). In the same experiment, cells were also incubated with 8 µg mL^{-1} functionalized AuNPs for 3 h, rinsed prior to being subjected to laser treatments at 250 Hz (80–100 mJ cm^{-2}) or 500 Hz (60–100 mJ cm^{-2}). The treatments at 250 Hz

(80–100 mJ cm^{-2}) or 500 Hz (60–80 mJ cm^{-2}) induced perforation of the targeted MDA-MB-231 and ARPE-19 cells, but they did not affect the non-targeted 661W cells (Fig. 5A–J). Interestingly, the laser treatment at the lowest fluence (60 mJ cm^{-2}, 500 Hz, 0.3 W) induced cell perforation of targeted cells and reduced slightly the cell viability (Fig. 5F and G). Within the 80–100 mJ cm^{-2} laser fluence range, increasing the laser repetition rate from 250 to 500 Hz decreased cell viability and increased cell perforation (Fig. 5A–E and H–M). At a laser fluence of 100 mJ cm^{-2}, targeted cells incubated with functionalized AuNPs were not perforated with a repetition rate of 100 Hz, whereas a repetition rate of 1 kHz destroyed cells even in the absence of AuNPs (data not shown). The smaller ARPE-19 cells were more sensitive to the laser treatment than the larger MDA-MB-231 cells in the presence of functionalized AuNPs (Table S5†). Thus, selective treatment of targeted cells with the laser at 250 Hz (80–100 mJ cm^{-2}) or 500 Hz (60–80 mJ cm^{-2}) can be achieved without affecting non-targeted cells. The threshold to observe selective optoporation was 49 pulses at 250 Hz (80 mJ cm^{-2}) or 97 pulses at 500 Hz (60 mJ cm^{-2}).

The lowest concentration of functionalized AuNPs for effective perforation of targeted MDA-MB-231 and ARPE-19 cells was evaluated next with the laser treatment at 500 Hz (60 mJ cm^{-2}) (Fig. S10†). For both cell lines, perforation did not occur when the AuNPs concentration was 2 μg mL^{-1}, or less (Fig. S10A–F†). Perforation of targeted cells increased as the concentration of Ab-functionalized AuNPs increased from 4 to 8 μg mL^{-1} (Fig. S10G–J†).

The selective optoporation of targeted MDA-MB-231 (Fig. 6A and B) and ARPE-19 (Fig. 6C and D) cells was then demonstrated with 8 μg mL^{-1} stable functionalized AuNPs enhancing off-resonance NIR fs laser (60 mJ cm^{-2}, 500 Hz) without affecting surrounding non-targeted 661W cells in co-culture (Fig. 7). Cells in the laser-irradiated area accumulated LY (green channel), while untreated cells remained non-perforated (Fig. 6A and C). The viability of irradiated cells stained with DAPI (blue channel) slightly decreased in comparison to the viability of untreated cells (Fig. 6A and C). Since non-targeted 661W cell membranes were stained with fluorescent tetramethylrhodamine dye conjugated to wheat germ agglutinin (WGA, red channel), the perforation of these cells would result in a colocalized staining (in yellow) by combining signals from the green and the red channels. The magnified central area of the micrographs shown for each combination of targeted cells co-cultured with non-targeted cells demonstrated that perforated cells were mainly targeted cells (Fig. 6B and D).

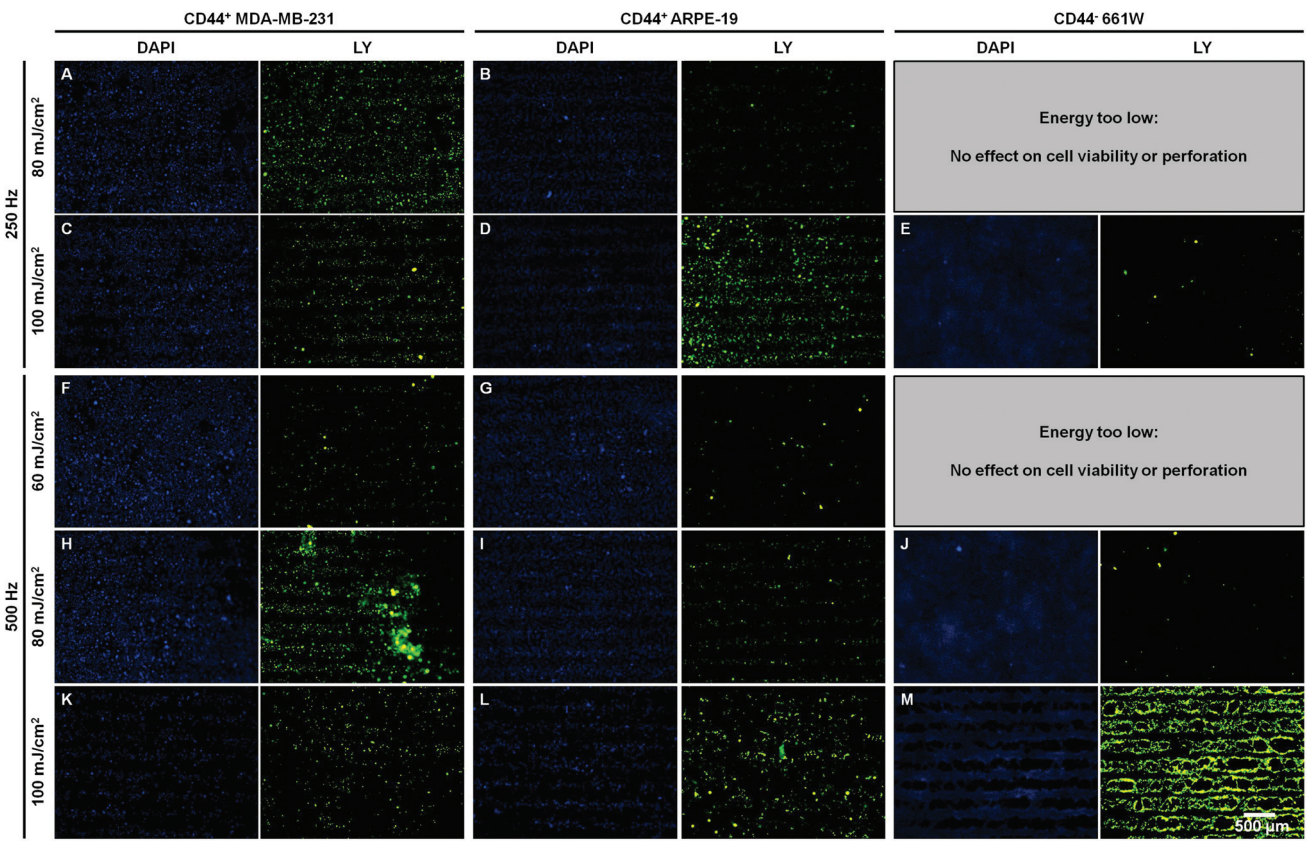

Fig. 5 Fluorescence imaging of laser-treated $CD44^+$ MDA-MB-231, $CD44^+$ ARPE-19 and $CD44^-$ 661W cells incubated for 3 h in DMEM/10% FBS/1% PS with 8 μg mL^{-1} AuNPs functionalized with OPSS-PEG-Ab (0.45%) during 1 h sequentially followed by HS-PEG (5 kDa) (A–M). LY (green) was added before laser treatment (60–100 mJ cm^{-2}, 250–500 Hz) and cell nuclei were stained with DAPI (blue). Representative images were obtained from two independent experiments.

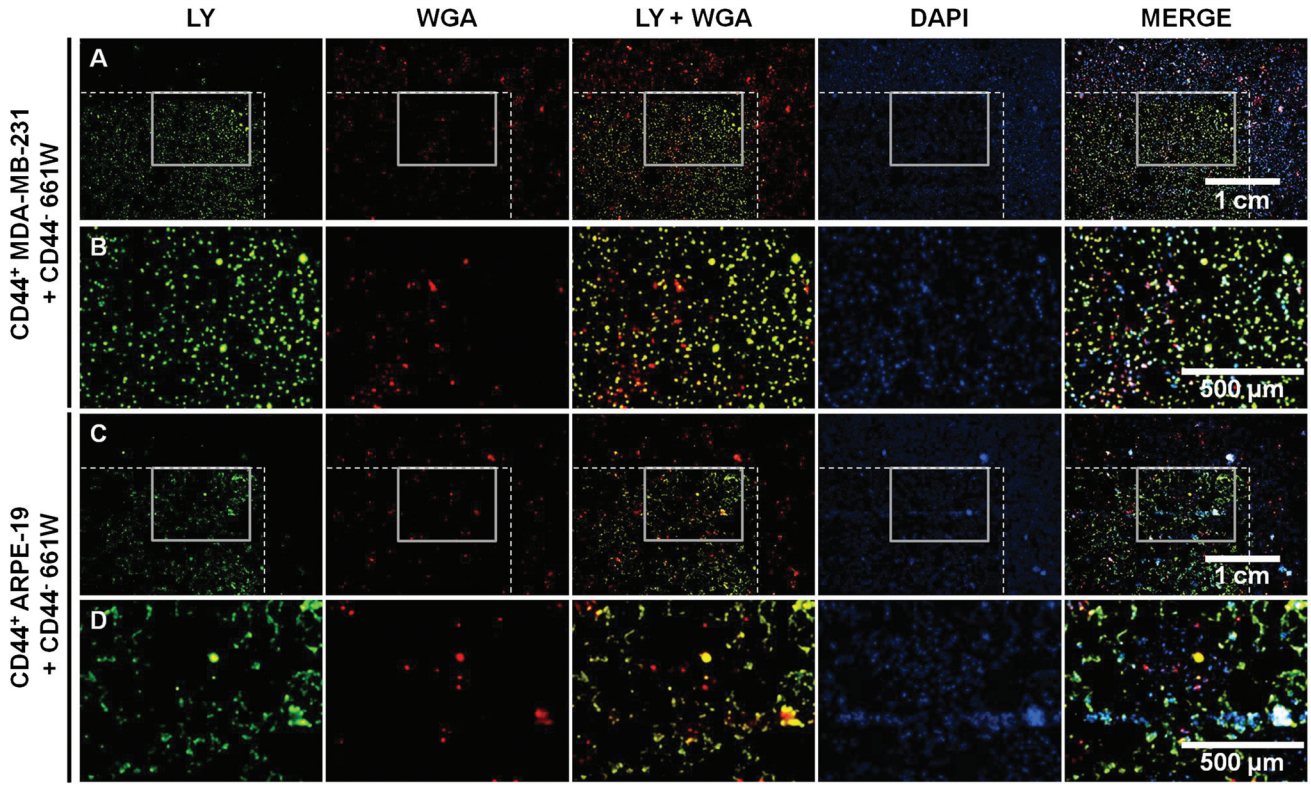

Fig. 6 Fluorescence imaging of laser-treated $CD44^+$ MDA-MB-231 (A,B) and $CD44^+$ ARPE-19 (C,D) cells in co-culture with $CD44^-$ 661W cells stained with WGA (red) incubated for 3 h in DMEM/10% FBS/1% PS with 8 µg mL^{-1} AuNPs functionalized with OPSS-PEG-Ab (0.45%) during 1 h sequentially followed by HS-PEG (5 kDa). LY (green) was added before laser treatment (60 mJ cm^{-2}, 500 Hz) and cell nuclei were stained with DAPI (blue). Representative images were obtained from two independent experiments. The laser-irradiated area is shown in the left box delimited with dashed line. The magnified central area from (A) and (C) are shown in (B) and (D), respectively.

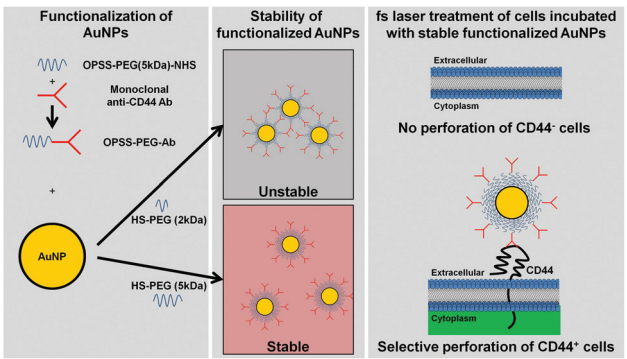

Fig. 7 Schematic representation of cell-specific optoporation with NIR fs laser and stable functionalized AuNPs. Stable colloidal AuNPs reflect red light while unstable aggregated AuNPs reflect blue light.

3. Experimental

3.1. Materials

Rat IgG2a monoclonal anti-human CD44 Abs (Hermes-1, 150 kDa) were purchased from abcam (Toronto, ON, Canada). OPSS-PEG(5 kDa)-NHS and HS-PEG (5 kDa) were purchased from Nanocs (New York, NY, U.S.A.). Citrate-capped AuNPs were purchased from Nanopartz (50 µg mL^{-1}, 100 nm in diameter, A11-100, Loveland, CO, U.S.A.) and stored at 4 °C in the dark to minimize photoinduced oxidation. Methanol was purchased from VWR International (Mississauga, ON, Canada). NaCl, Na_2CO_3, HS-PEG (2 kDa), PBS, fluorescent LY, fluorescent DAPI and trypan blue solution (0.4%) were obtained from Sigma-Aldrich (Oakville, ON, Canada) and used without further purification. DMEM (containing 4.5 g L^{-1} D-glucose, 584 mg L^{-1} L-glutamine and 110 mg L^{-1} sodium pyruvate), DMEM/nutrient mixture F-12 (DMEM/F-12 containing 3.15 g L^{-1} D-glucose, 365 mg L^{-1} L-glutamine and 55 mg L^{-1} sodium pyruvate), penicillin 10 000 units per mL, streptomycin 10 000 µg mL^{-1}, trypsin 0.25%-EDTA, FBS, fluorescent WGA and fluorescent Alexa Fluor 488 dye conjugated to goat anti-rat IgG (H + L) Abs were purchased from Life Technologies (Burlington, ON, Canada). Normal goat serum was purchased from Jackson ImmunoResearch Laboratories (West Grove, PA, U.S.A.). Vectashield mounting medium for fluorescence was purchased from Vector Laboratories (Burlingame, CA, U.S.A.). Water was purified with a Millipore treatment system (18.2 MΩcm, Etobicoke, ON, Canada).

3.2. Antibody conjugation to OPSS-PEG-NHS

The anti-CD44 Abs stored in PBS (100 µL, 1.163 mg mL^{-1}) were diluted in aqueous Na_2CO_3 10 mM pH 8.5 (1.02 mL), and

quickly added to a filtered solution of OPSS-PEG-NHS diluted in Na_2CO_3 10 mM pH 8.5 (124 μL, 58.9 μg mL^{-1}). The reaction mixture (1.244 mL, 100 μg mL^{-1}, Ab : OPSS-PEG-NHS molar ratio: 1 : 1.88) was vortexed briefly and kept at 4 °C for 3 h. Aliquots of the solution were kept at −20 °C until use.

3.3. Functionalization of AuNPs

3.3.1. Optimization of HS-PEG concentration. HS-PEG (2 or 5 kDa) was diluted from 1 mg mL^{-1} to 10 ng mL^{-1} in water. A suspension of citrate-capped AuNPs (450 μL, 50 μg mL^{-1}) in DI water was treated with an aqueous solution of HS-PEG (50 μL) or water (50 μL, control reaction). The mixtures were vortexed and kept for 1 h at 4 °C. Subsequently, they were treated with either water (55 μL) or a 10% (w/v) aqueous NaCl solution (55 μL). The mixtures were kept at 4 °C for 30 min or 24 h. An aliquot of each sample (250 μL) was placed in a 96-well plate for analysis by UV-visible-NIR spectroscopy.

3.3.2. Optimization of mixture conditions and OPSS-PEG-Ab concentration. AuNPs were prepared by following a procedure reported previously[13,29] with modifications. An aqueous solution of citrate-capped AuNPs (2 mL, 50 μg mL^{-1}) was treated with aqueous Na_2CO_3 10 mM pH 8.5 (222, 218.667, 212 or 202 μL) and a solution of OPSS-PEG-Ab (0, 3.333, 10 or 20 μL, 100 μg mL^{-1}) to reach a volume of 2.222 mL. Simultaneously, or after 1 h incubation at 4 °C, an aqueous solution of 50 μM HS-PEG (2 or 5 kDa, 247 μL) was added to the suspensions of AuNPs-PEG-Ab. Water or HS-PEG was also added to suspensions of AuNPs prepared under the same conditions (2 mL AuNPs treated with 222 μL Na_2CO_3 10 mM pH 8.5). After 1 h incubation at 4 °C, two samples (320 μL) were taken for analysis. A sample (1.829 mL) was subjected to centrifugation at 4610 g during 2 min. The supernatant was then removed and replaced with 1.48 mL phenol red-free DMEM. Aliquots of the resulting mixtures (320 μL) were treated with water or 10% NaCl (35.5 μL) at 4 °C during 30 min and analyzed by UV-visible-NIR spectroscopy in a 96-well plate.

3.4. UV-visible-NIR spectroscopy measurements

UV-visible-NIR absorption spectra (300 to 900 nm, 2 nm step) were acquired with an Epoch microplate spectrophotometer (BioTek Instruments, Winooski, VT, U.S.A.) controlled with the Gen5 Data Analysis software version 1.11.5. A blank spectrum (solvent without AuNPs) was subtracted from each sample spectrum. The colloidal AuNP size and concentration were determined from the absorbance at 450 nm and the wavelength of the plasmon peak ($\varepsilon = 1.1 \times 10^{11}$ M^{-1} cm^{-1}).[39]

3.5. Zeta potential measurements

An aqueous solution of citrate-capped AuNPs (2 mL, 50 μg mL^{-1}) was treated with aqueous Na_2CO_3 10 mM pH 8.5 (212 μL) and a solution of OPSS-PEG-Ab (10 μL, 100 μg mL^{-1}). After 1 h incubation at 4 °C, an aqueous solution of 50 μM HS-PEG (2 or 5 kDa, 247 μL) was added to the suspensions of AuNPs-PEG-Ab. Water or HS-PEG was also added to suspensions of AuNPs prepared under the same conditions (2 mL AuNPs treated with 222 μL Na_2CO_3 10 mM pH 8.5). After 1 h incubation at 4 °C, samples (1 mL) were taken for analysis. The dispersions of 40.5 μg mL^{-1} AuNPs were degassed. The zeta potential of AuNPs (750 μL) was measured at 4, 20 and 37 °C with a ZetaSizer Nano series ZS from Malvern Instruments (Worcestershire, U.K.) equipped with a 4 mW He–Ne laser operating at 633 nm. The measurements were performed at an angle of 173° for samples heated from 4 to 37 °C and back, using a 5 min equilibrating time before the measurement series, and a 5 min equilibration time at each temperature point. Three measurements were conducted at each temperature and an average of these measurements is reported for each experiment.

3.6. Cell culture

Human MDA-MB-231 breast cancer, human ARPE-19 retinal pigmented epithelium and mouse 661W photoreceptor cell lines (American Type Culture Collection, Manassas, VA, U.S.A.) were cultured at 5000 cells per cm^2 in cell culture-treated polystyrene T75 flasks (Sarstedt, Saint-Léonard, QC, Canada). MDA-MB-231 and 661W cells were grown in DMEM supplemented with 10% FBS and antibiotics (100 units per mL penicillin and 100 μg mL^{-1} streptomycin, 1% PS) and ARPE-19 cells were grown in DMEM/F-12 supplemented with 10% FBS/1% PS in a humidified incubator at 37 °C under a 5% CO_2 atmosphere. Confluent cells were removed by trypsinization and seeded for experiments in DMEM or DMEM/F-12 supplemented with 10% FBS/1% PS.

3.7. Darkfield and fluorescence imaging

Cells were seeded onto 19.625 cm^2 glass bottom dishes (5000 cells per cm^2, MatTek, Ashland, MA, U.S.A.). At 80–90% confluence, cells were washed once with PBS before adding AuNPs diluted to 8 μg mL^{-1} in DMEM/10% FBS/1% PS.[8] After 3 h incubation at 37 °C, cells were washed three times with PBS and fixed with ice-cold methanol during 10 min at 20 °C. All subsequent steps were followed by three PBS washes. Nuclei were stained with 2.5 μg mL^{-1} DAPI during 5 min at 20 °C. In some experiments, samples were incubated for 1.5 h with 10% (v/v) normal goat serum diluted in PBS at 20 °C, then with 0.5% (v/v) Alexa Fluor 488 dye conjugated to goat anti-rat IgG Abs during 1.5 h. Samples were examined with an Eclipse Ti microscope (Nikon, Mississauga, ON, Canada) equipped with a 4× objective (numerical aperture (NA) = 0.13, Nikon), a 20× objective (NA = 0.45, Nikon), a 60× objective (NA = 0.7, Nikon), an available additional 1.5× magnification, a darkfield condenser (NA = 0.95–0.8, Nikon), different filters (ET-DAPI (ex 350 ± 25, em 460 ± 25), ET-GFP (ex 470 ± 20, em 525 ± 25), ET-DsRED (ex 545 ± 15, em 620 ± 30), Chroma Technology, Bellows Falls, VT, U.S.A.), a fluorescent lamp C-HGFI Intensilight (Nikon) and a QIClick digital CCD camera (QImaging, Surrey, BC, Canada). Pictures were taken with the NIS-Elements BR microscope imaging software version 4.00.03 (Nikon). Darkfield images were taken with three different filters (ET-DAPI, ET-GFP and ET-DsRED) and merged with the fluorescence image.

3.8. Immunofluorescence

MDA-MB-231, ARPE-19 and 661W cells were grown in 8-well glass chamber slides (75 000 cells per well, BD Biosciences, Mississauga, ON, Canada). After 2 days, cells were washed once with PBS, fixed with ice-cold 70% methanol/30% acetone for 5 min or 4% paraformaldehyde/96% PBS for 10 min. The samples were blocked with 10% normal goat serum diluted in PBS for 1 h at 20 °C. All subsequent steps were followed by three PBS washes. The cells were incubated for 1.5 h with 1% (v/v) anti-CD44 Abs or 2% (v/v) OPSS-PEG-Ab. Then, 1% Alexa Fluor 488 dye conjugated to goat anti-rat IgG Abs were incubated with the cells for 1.5 h. The cell nuclei were stained with 2.5 μg mL^{-1} DAPI for 5 min and the slides mounted with Vectashield. Samples were examined and pictures were taken as described above using fluorescence microscopy.

3.9. Flow cytometry

Cells grown as above in 19.625 cm^2 glass bottom dishes were incubated for 3 h with 8 μg mL^{-1} AuNPs in DMEM/10% FBS/1% PS. Then, cells were washed three times with PBS, detached with 1.3 mL trypsin during 10 min and neutralized with 0.15 mL FBS. A sample (100 μL) was mixed with trypan blue (50 μL) to evaluate cell viability using a hemacytometer (Hausser Scientific, Horsham, PA, U.S.A.). Forward scatter and side scatter signals from a He–Ne laser operating at 633 nm without filter were assessed with a BD LSR II flow cytometer (BD Biosciences) with the acquisition of a minimum of 10 000 events from each sample (1 mL).

3.10. Scanning electron microscopy (SEM)

Cells grown as above in 19.625 cm^2 glass bottom dishes were incubated for 3 h with 8 μg mL^{-1} AuNPs in DMEM/10% FBS/1% PS. Then, cells were washed three times with PBS, fixed in 5% glutaraldehyde/95% PBS for 30 min, and incubated for 30 min in 5% glutaraldehyde/95% water. The samples were then washed three times with distilled water and dried overnight under a biological hood. Samples were sputter-coated for 15 seconds at 10 mA with a 5 nm uniform gold layer (Polaron SC502 Sputter Coater, Polaron Instruments, Watford, U.K.). The samples were observed with a Hitachi S-4700 Field Emission SEM version II (Hitachi High-Technologies, Toronto, ON, Canada) with the acquisition software quartz PCI (Hitachi). SEM images were captured at 8 kV, 20 000× magnification and a working distance of 14.8–15 mm. The number of AuNPs was counted for each cell by considering the average cell size evaluated previously by fluorescence microscopy.

3.11. Laser treatment

Cells grown as above in 19.625 cm^2 glass bottom dishes were incubated for 3 h with 1–8 μg mL^{-1} functionalized AuNPs in DMEM/10% FBS/1% PS. Then, cells were washed three times with PBS. Phenol red-free DMEM containing 10% FBS (1.9 mL) and 6 mM LY (0.1 mL) were added to each dish. The laser treatment was performed by using a Ti:Sapphire laser (Spitfire, Spectra Physics, Mountain View, CA, U.S.A.) delivering 45 fs NIR pulses at a central wavelength of 800 nm, a repetition rate of 1 kHz (that can be reduced to 100, 250 and 500 Hz), and maximum output energy of 6 mJ per pulse. The laser beam attenuated by a Brewster window and a polarizer was delivered to the sample using a plano-convex lens (focal length f = 75 mm). The sample was irradiated from below with a slightly focused laser beam having a Gaussian profile and a spot diameter of 680 μm (defined at $1/e^2$) at the sample plane. A three axis motorized translation stage performed the displacement of the sample to ensure irradiation over a 5 mm × 5 mm area with a scanning velocity of 3.5 mm s^{-1} and a line to line step-size of 300 μm (44% of the laser spot diameter). The laser treatment took about 1 min per dish. Negative controls (laser irradiation in identical conditions but without AuNPs) were also performed. Two hours after the laser treatment, cells were washed three times with PBS to remove extracellular LY. Afterwards, cells were fixed with ice-cold methanol during 10 min at 20 °C, washed three times with PBS, then incubated for 5 min with 2.5 μg mL^{-1} DAPI (2 mL) and washed three times with PBS. The cells were then stored at 4 °C. In co-culture experiments, non-targeted 661W cells stained with WGA and targeted (MDA-MB-231 or ARPE-19) cells were seeded in a 1 : 5 ratio. Observation of the perforated cells (LY, green fluorescence) and of the total number of cells (DAPI, blue fluorescence) was performed using fluorescence microscopy. Samples were examined and pictures were taken as described above. Negative controls (area without laser irradiation) were also observed for each dish.

3.12. Statistical analysis

Results are expressed as means ± standard deviation (SD) in all experiments. Statistical computations were performed with GraphPad Instat 3.00 software (GraphPad Software, San Diego, CA, U.S.A.). The Tukey-Kramer multiple comparison test (ANOVA) was used. Values were considered significantly different if $p < 0.05$.

4. Conclusions

In summary, the selective cell optoporation with stable functionalized AuNPs enhanced NIR ultrafast laser pulse irradiation offers a highly versatile method where targeted cells could be treated and surrounding non-targeted cells would remain viable. The AuNPs sequentially functionalized with mixed PEG layers and monoclonal anti-CD44 Abs are stable in cell culture medium containing serum proteins. This novel treatment can be adapted to target and perforate other cell types simply by changing the biomarkers. Indeed, preliminary data show that the laser treatment of transfected cells expressing recombinant HA-tagged proteins in a heterogeneous population can be selectively targeted and perforated with stable 100 nm AuNPs functionalized sequentially with OPSS-PEG(5 kDa)-NHS conjugated to monoclonal anti-HA Abs, followed by HS-PEG (5 kDa). The tool would be suitable for *in vivo* applications since biological tissues absorb very weakly the energy in the NIR range.

The developed non-invasive technology requires no surgery, thus preventing complications such as pain, anaesthesia effects, infection, blood clots, fatigue and lack of energy. Moreover, this technology can provide an invaluable tool for treating patients with diseases with defective cells, such as cancer, a major public health issue in the Western world.

Acknowledgements

This work was supported by Le Fonds de recherche du Québec, Consortium québécois sur la découverte du médicament (CQDM), the Natural Science and Engineering Research Council of Canada (NSERC) and Canadian Institutes of Health Research (CIHR). EB received funding from Fonds de recherche du Québec – Santé and CB acknowledges funding from the EU under a Marie Curie Fellowship, FP7-PEOPLE-2013-IOF, project reference 624888. David Rioux, Sergiy Patskovsky, Rémi Lachaine, Alexandra Thibeault-Eybalin, Ariel Wilson, Flavie Lavoie-Cardinal and Yves Drolet are acknowledged for technical assistance and fruitful discussions. The authors also thank Danièle Gagné and Gaël Dulude from the IRIC flow cytometry platform for assistance with flow cytometry.

References

1 Y.-S. Chen, Y.-C. Hung, I. Liau and G. S. Huang, *Nanoscale Res. Lett.*, 2009, **4**, 858–864; E. E. Connor, J. Mwamuka, A. Gole, C. J. Murphy and M. D. Wyatt, *Small*, 2005, **1**, 325–327; P. D. Howes, R. Chandrawati and M. M. Stevens, *Science*, 2014, **346**, 1247390; X. Huang, P. K. Jain, I. H. El-Sayed and M. A. El-Sayed, *Nanomedicine*, 2007, **2**, 681–693; J. A. Khan, B. Pillai, T. K. Das, Y. Singh and S. Maiti, *ChemBioChem*, 2007, **8**, 1237–1240; R. Shukla, V. Bansal, M. Chaudhary, A. Basu, R. R. Bhonde and M. Sastry, *Langmuir*, 2005, **21**, 10644–10654; K. Weintraub, *Nature*, 2013, **495**, S14–S16.

2 S. Kumar, J. Aaron and K. Sokolov, *Nat. Protoc.*, 2008, **3**, 314–320.

3 G. Mie, *Ann. Phys.*, 1908, **330**, 377–445.

4 E. Boulais, R. Lachaine, A. Hatef and M. Meunier, *J. Photochem. Photobiol., C*, 2013, **17**, 26–49.

5 W. Ding, E. Bergeron, R. Lachaine and M. Meunier, in *Applications of Nanoscience in Photomedicine*, ed. M. R. Hamblin and P. Avci, Woodhead Publishing, Sawston (U.K.), 2015, ch. 16, pp. 331–376; B. Feng, Z. Xu, F. Zhou, H. Yu, Q. Sun, D. Wang, *et al.*, *Nanoscale*, 2015, **7**, 14854–14864; E. Y. Lukianova-Hleb, A. Belyanin, S. Kashinath, X. Wu and D. O. Lapotko, *Biomaterials*, 2012, **33**, 1821–1826; E. Y. Lukianova-Hleb, X. Ren, P. E. Constantinou, B. P. Danysh, D. L. Shenefelt, D. D. Carson, *et al.*, *PLoS One*, 2012, **7**, e34537; E. Y. Lukianova-Hleb, X. Ren, R. R. Sawant, X. Wu, V. P. Torchilin and D. O. Lapotko, *Nat. Med.*, 2014, **20**, 778–784; E. Y. Lukianova-Hleb, X. Ren, J. A. Zasadzinski, X. Wu and D. O. Lapotko, *Adv. Mater.*, 2012, **24**, 3831–3837; E. Y. Lukianova-Hleb, D. S. Wagner, M. K. Brenner and D. O. Lapotko, *Biomaterials*, 2012, **33**, 5441–5450; M. S. Noh, S. Lee, H. Kang, J.-K. Yang, H. Lee, D. Hwang, *et al.*, *Biomaterials*, 2015, **45**, 81–92; T. Patino, U. Mahajan, R. Palankar, N. Medvedev, J. Walowski, M. Münzenberg, *et al.*, *Nanoscale*, 2015, **7**, 5328–5337; B. St-Louis Lalonde, É. Boulais, J.-J. Lebrun and M. Meunier, *Biomed. Opt. Express*, 2013, **4**, 490–499; D. S. Wagner, N. A. Delk, E. Y. Lukianova-Hleb, J. H. Hafner, M. C. Farach-Carson and D. O. Lapotko, *Biomaterials*, 2010, **31**, 7567–7574; D. Wang, Z. Xu, H. Yu, X. Chen, B. Feng, Z. Cui, *et al.*, *Biomaterials*, 2014, **35**, 8374–8384; X. Wu, J.-Y. Chen, A. Brech, C. Fang, J. Wang, P. J. Helm, *et al.*, *Biomaterials*, 2013, **34**, 6157–6162; R. Xiong, K. Raemdonck, K. Peynshaert, I. Lentacker, I. De Cock, J. Demeester, *et al.*, *ACS Nano*, 2014, **8**, 6288–6296; J. Zhou, Z. Wang, Q. Li, F. Liu, Y. Du, H. Yuan, *et al.*, *Nanoscale*, 2015, **7**, 5869–5883.

6 R. Weissleder, *Nat. Biotechnol.*, 2001, **19**, 316–317.

7 É. Boulais, R. Lachaine and M. Meunier, *Nano Lett.*, 2012, **12**, 4763–4769.

8 J. Baumgart, L. Humbert, É. Boulais, R. Lachaine, J.-J. Lebrun and M. Meunier, *Biomaterials*, 2012, **33**, 2345–2350.

9 A. A. Davis, M. J. Farrar, N. Nishimura, M. M. Jin and C. B. Schaffer, *Biophys. J.*, 2013, **105**, 862–871.

10 M. Schomaker, D. Heinemann, S. Kalies, S. Willenbrock, S. Wagner, I. Nolte, *et al.*, *J. Nanobiotechnol.*, 2015, **13**, 10; M. Schomaker, D. Killian, S. Willenbrock, D. Heinemann, S. Kalies, A. Ngezahayo, *et al.*, *J. Biophotonics*, 2015, **8**, 646–658.

11 J. V. Jokerst, T. Lobovkina, R. N. Zare and S. S. Gambhir, *Nanomedicine*, 2011, **6**, 715–728.

12 G. A. Craig, P. J. Allen and M. D. Mason, in *Methods in Molecular Biology*, ed. S. R. Grobmyer and B. M. Moudgil, Cancer Nanotechnology, Humana Press, Totowa (NJ, U.S.A.), 2010, ch. 12, vol. 624, pp. 177–193; H. Ju, X. Zhang and J. Wang, in *NanoBiosensing: Principles, Development and Application*, ed. H. Ju, X. Zhang and J. Wang, Springer, New York (NY, U.S.A.), 2011, ch. 1, pp. 1–38.

13 L. R. Hirsch, N. J. Halas and J. L. West, in *Methods in Molecular Biology*, ed. S. J. Rosenthal and D. W. Wright, Nano-Biotechnology Protocols, Humana Press, Totowa (NJ, U.S.A.), 2005, ch. 8, vol. 303, pp. 101–111.

14 J. Gao, X. Huang, H. Liu, F. Zan and J. Ren, *Langmuir*, 2012, **28**, 4464–4471; L. L. Ma, J. O. Tam, B. W. Willsey, D. Rigdon, R. Ramesh, K. Sokolov, *et al.*, *Langmuir*, 2011, **27**, 7681–7690.

15 N. Chattopadhyay, Z. Cai, J.-P. Pignol, B. Keller, E. Lechtman, R. Bendayan, *et al.*, *Mol. Pharm.*, 2010, **7**, 2194–2206.

16 A. R. Lowery, A. M. Gobin, E. S. Day, N. J. Halas and J. L. West, *Int. J. Nanomed.*, 2006, **1**, 149–154.

17 B. Van de Broek, N. Devoogdt, A. D'Hollander, H.-L. Gijs, K. Jans, L. Lagae, *et al.*, *ACS Nano*, 2011, **5**, 4319–4328.

18 T. Liu and B. Thierry, *Langmuir*, 2012, **28**, 15634–15642.
19 W. Eck, G. Craig, A. Sigdel, G. Ritter, L. J. Old, L. Tang, *et al.*, *ACS Nano*, 2008, **2**, 2263–2272.
20 E. I. Galanzha, J.-W. Kim and V. P. Zharov, *J. Biophotonics*, 2009, **2**, 725–735; K. Lee, V. P. Drachev and J. Irudayaraj, *ACS Nano*, 2011, **5**, 2109–2117.
21 E. Lee, Y. Hong, J. Choi, S. Haam, J.-S. Suh, Y.-M. Huh, *et al.*, *Nanotechnology*, 2012, **23**, 465101.
22 J. I. Fletcher, M. Haber, M. J. Henderson and M. D. Norris, *Nat. Rev. Cancer*, 2010, **10**, 147–156; L. Vermeulen, F. de Sousa e Melo, D. J. Richel and J. P. Medema, *Lancet Oncol.*, 2012, **13**, e83–e89.
23 R. K. Ambasta, A. Sharma and P. Kumar, *Vasc. Cell*, 2011, **3**, 26.
24 S. A. Mani, W. Guo, M.-J. Liao, E. N. Eaton, A. Ayyanan, A. Y. Zhou, *et al.*, *Cell*, 2008, **133**, 704–715; M. Shipitsin, L. L. Campbell, P. Argani, S. Weremowicz, N. Bloushtain-Qimron, J. Yao, *et al.*, *Cancer Cell*, 2007, **11**, 259–273.
25 M. H. El-Dakdouki, E. Puré and X. Huang, *Nanoscale*, 2013, **5**, 3895–3903; V. M. Platt and F. C. Szoka Jr., *Mol. Pharm.*, 2008, **5**, 474–486; M. Zöller, *Nat. Rev. Cancer*, 2011, **11**, 254–267.
26 M. Al-Hajj, M. S. Wicha, A. Benito-Hernandez, S. J. Morrison and M. F. Clarke, *Proc. Natl. Acad. Sci. U. S. A.*, 2003, **100**, 3983–3988.
27 E. Olsson, G. Honeth, P.-O. Bendahl, L. H. Saal, S. Gruvberger-Saal, M. Ringnér, *et al.*, *BMC Cancer*, 2011, **11**, 418.
28 C. Sheridan, H. Kishimoto, R. K. Fuchs, S. Mehrotra, P. Bhat-Nakshatri, C. H. Turner, *et al.*, *Breast Cancer Res.*, 2006, **8**, R59.
29 S. Patskovsky, E. Bergeron and M. Meunier, *J. Biophotonics*, 2015, **8**, 162–167; S. Patskovsky, E. Bergeron, D. Rioux and M. Meunier, *J. Biophotonics*, 2015, **8**, 401–407.
30 A. Leifert, Y. Pan-Bartnek, U. Simon and W. Jahnen-Dechent, *Nanoscale*, 2013, **5**, 6224–6242; G. Maiorano, S. Sabella, B. Sorce, V. Brunetti, M. A. Malvindi, R. Cingolani, *et al.*, *ACS Nano*, 2010, **4**, 7481–7491; A. E. Nel, L. Mädler, D. Velegol, T. Xia, E. M. V. Hoek, P. Somasundaran, *et al.*, *Nat. Mater.*, 2009, **8**, 543–557; A. Salvati, A. S. Pitek, M. P. Monopoli, K. Prapainop, F. B. Bombelli, D. R. Hristov, *et al.*, *Nat. Nanotechnol.*, 2013, **8**, 137–143.
31 K. Park and Y. Lee, *J. Toxicol. Environ. Health, Part A*, 2013, **76**, 1236–1245.
32 L. Duchesne, D. Gentili, M. Comes-Franchini and D. G. Fernig, *Langmuir*, 2008, **24**, 13572–13580; J. Manson, D. Kumar, B. J. Meenan and D. Dixon, *Gold Bull.*, 2011, **44**, 99–105; F. Schulz, T. Vossmeyer, N. G. Bastús and H. Weller, *Langmuir*, 2013, **29**, 9897–9908; K. A. Willets and R. P. Van Duyne, *Annu. Rev. Phys. Chem.*, 2007, **58**, 267–297.
33 W. P. Wuelfing, S. M. Gross, D. T. Miles and R. W. Murray, *J. Am. Chem. Soc.*, 1998, **120**, 12696–12697.
34 E. Casals, T. Pfaller, A. Duschl, G. J. Oostingh and V. Puntes, *ACS Nano*, 2010, **4**, 3623–3632.
35 J. G. Morton, E. S. Day, N. J. Halas and J. L. West, in *Methods in Molecular Biology*, ed. S. R. Grobmyer and B. M. Moudgil, Cancer Nanotechnology, Humana Press, Totowa (NJ, U.S.A.), 2010, ch. 7, vol. 624, pp. 101–117.
36 E. C. Cho, Q. Zhang and Y. Xia, *Nat. Nanotechnol.*, 2011, **6**, 385–391.
37 X. Yu, J. Wang, A. Feizpour and B. M. Reinhard, *Anal. Chem.*, 2013, **85**, 1290–1294.
38 C. Boutopoulos, E. Bergeron and M. Meunier, *J. Biophotonics*, DOI: 10.1002/jbio.201500135, in press.
39 W. Haiss, N. T. K. Thanh, J. Aveyard and D. G. Fernig, *Anal. Chem.*, 2007, **79**, 4215–4221.